Electron-spin spectral diffusion in an erbium doped crystal at millikelvin temperatures

M. Rančić,[1,*] M. Le Dantec,[1,*] S. Lin,[2] S. Bertaina,[3] T. Chanelière,[4] D. Serrano,[5] P. Goldner,[5] R. B. Liu,[2] E. Flurin,[1] D. Estève,[1] D. Vion,[1] and P. Bertet[1,†]

[1]*Université Paris-Saclay, CEA, CNRS, SPEC, 91191 Gif-sur-Yvette Cedex, France*

[2]*Department of Physics, Centre for Quantum Coherence, and The Hong Kong Institute of Quantum Information Science and Technology, The Chinese University of Hong Kong, Shatin, New Territories, Hong Kong, China*

[3]*CNRS, Aix-Marseille Université, IM2NP, UMR 7334, Institut Matériaux Microélectronique et Nanosciences de Provence, 13013 Marseille, France*

[4]*Université Grenoble Alpes, CNRS, Grenoble INP, Institut Néel, 38000 Grenoble, France*

[5]*Chimie ParisTech, PSL University, CNRS, Institut de Recherche de Chimie Paris, 75005 Paris, France*

(Received 5 April 2022; accepted 9 September 2022; published 11 October 2022)

Erbium doped crystals offer a versatile platform for hybrid quantum devices because they combine magnetically sensitive electron-spin transitions with telecom-wavelength optical transitions. At the high doping concentrations necessary for many quantum applications, however, strong magnetic interactions of the electron-spin bath lead to excess spectral diffusion and rapid decoherence. Here we lithographically fabricate a 4.4 GHz superconducting planar microresonator on a $CaWO_4$ crystal doped with Er ions at a concentration of 20 ppm relative to Ca. Using the microwave resonator, we characterize the spectral diffusion processes that limit the electron-spin coherence of Er ions at millikelvin temperatures by applying two- and three-pulse echo sequences. The coherence time shows a strong temperature dependence, reaching 1.3 ms at 23 mK for an electron-spin transition of ^{167}Er.

DOI: 10.1103/PhysRevB.106.144412

I. INTRODUCTION

Rare-earth ion doped materials cooled to liquid helium temperatures have demonstrated long coherence times [1–4] and large efficiencies for quantum memory demonstrations in the optical domain [5–7]. Recently, interest in these materials has extended to subkelvin temperatures and subtesla fields, where the electron-spin transitions of Kramers (odd electron number) rare-earth ions achieve gigahertz frequencies while exceeding the energy of the thermal bath. This interest is motivated by the prospect of ensemble-based microwave-to-optical conversion [8,9] and microwave quantum memories [10,11], both of which require long electron-spin coherence times and sufficient concentration for high-fidelity operation. Previous demonstrations of ensemble-based microwave quantum memories required concentrations of electron spins between 1 and 100 ppm to achieve storage efficiencies of order 10^{-3} [12–14]. However, greater efficiencies will be needed to overcome the threshold for fault-tolerant communication (0.96) [15] and computation (0.99) [16], likely requiring higher spin concentrations or narrower absorption linewidths.

Several rare-earth doped materials have also demonstrated millisecond-scale electron-spin coherence [17,18] and hybridized electron-nuclear-spin coherence [19,20] with these applications in mind. Among these proposed materials, erbium doped calcium tungstate (Er^{3+}:$CaWO_4$) has emerged as a leading candidate due to its telecom-wavelength optical transition and ∼20 ms coherence both predicted [21,22] and measured [21] on a magnetically sensitive electron-spin transition. This demonstration of long coherence was attributed to a millikelvin spin-bath temperature combined with an ultralow Er doping concentration of just 0.7 ppb, yielding a regime in which the weak magnetic interaction with the ^{183}W nuclear-spin bath dictated the electron-spin decoherence rate.

At higher doping concentrations that are required for quantum applications, however, the strong magnetic interactions between the electron spins of erbium ions are expected to induce faster decoherence due to spectral diffusion (SD) [23]. Here we use pulsed electron spin resonance (ESR) spectroscopy to investigate SD in 20 ppm Er doped $CaWO_4$ in the millikelvin temperature regime. Moreover, we demonstrate a two-pulse echo coherence time of 1.3 ms for an electron-spin transition of Er at 4.4 GHz and determine that this coherence is limited by unwanted paramagnetic impurities, indicating that Er:$CaWO_4$ could be suitable for quantum information processing applications requiring large optical or microwave absorption.

II. STRUCTURE OF Er^{3+}:$CaWO_4$

Calcium tungstate is an optically transparent crystal with a tetragonal unit cell structure (space group $I4_1/a$) and orthogonal crystal axes a, b, and c. An illustration of the unit cell structure is presented in Fig. 1(a) which has dimensions $5.2 \times 5.2 \times 11.4$ Å parallel to the crystal $a \times b \times c$ axes.

*These authors contributed equally to this work.
†patrice.bertet@cea.fr

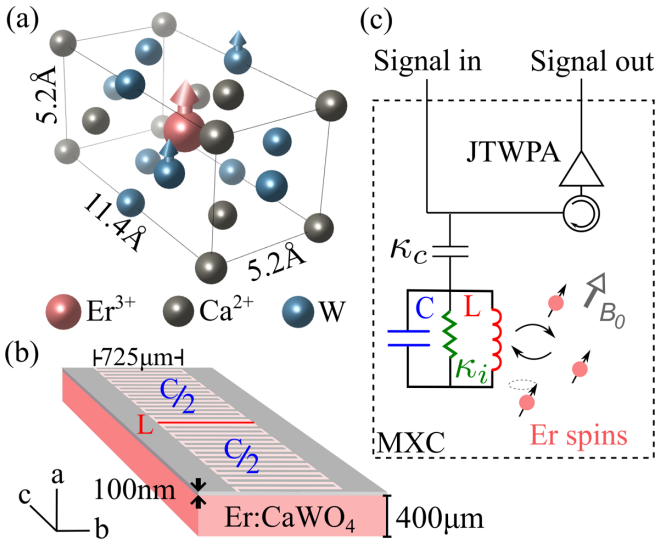

FIG. 1. Experimental setup. (a) Unit cell of $CaWO_4$ showing a central Er dopant. Oxygen atoms were removed for clarity. (b) Three-dimensional perspective view of an Er^{3+}:$CaWO_4$ crystal, showing the thin-film Nb resonator patterned on the surface. Crystal axes relevant to (a) and (b) are shown in the bottom left corner. (c) Experimental ESR setup, comprising the resonator and JTWPA.

Crystals grown with a natural abundance of isotopes exhibit an intrinsically low level of magnetic noise, which originates almost exclusively from the nuclear spins of the ^{183}W isotope. This isotope has a natural abundance of 14% and a nuclear spin-1/2 moment with a relatively small gyromagnetic ratio of $\gamma_W/2\pi = 1.8$ MHz/T. For this reason $CaWO_4$ is considered one of the best candidate hosts for quantum information processing among thousands of known materials [22,24].

In the crystalline matrix, the Er^{3+} ions substitutionally replace Ca^{2+} ions with additional long-range charge compensation [25]. The electrostatic interaction between the Er ions and the $CaWO_4$ matrix lifts the 16-fold degeneracy of the $J = 15/2$ electronic ground state of trivalent erbium, leading to eight pairs of degenerate electronic sublevels known as Kramers doublets. Each doublet forms an effective spin-1/2 system, and only the lowest-energy Kramers doublet (Z_1) is populated at millikelvin temperatures. The first excited-state doublet Z_2 has an additional energy of 19.2 cm^{-1}, corresponding to an excitation frequency of 575 GHz, while the entire $^4I_{15/2}$ manifold has an energy span of 319.4 cm^{-1} from Z_1 to Z_8 [26]. In the presence of an applied magnetic field B_0, the effective electron spin of the Z_1 doublet shows a strongly anisotropic Zeeman effect, characterized by the Hamiltonian

$$H_Z = \mu_B \mathbf{S} \cdot \mathbf{g} \cdot \mathbf{B_0}.$$

Here μ_B is the Bohr magneton, and $\mathbf{g}$ is the g tensor whose symmetry mirrors the tetragonal S_4 point-group symmetry of the crystal electric field at the location of the Er ion [27]:

$$\mathbf{g} = \begin{bmatrix} 8.38 & 0 & 0 \\ 0 & 8.38 & 0 \\ 0 & 0 & 1.247 \end{bmatrix}_{(a,b,c)}.$$

This effective-spin Hamiltonian applies only to the isotopes of Er that have no nuclear spin ($I = 0$ isotopes), comprising predominantly ^{166}Er, ^{168}Er, and ^{170}Er. While these represent 77% of the naturally occurring isotopes of Er, the other 23% of Er ions belong to the ^{167}Er isotope, which has nuclear spin $\mathbf{I} = 7/2$. For this subset of ions the magnetic hyperfine interaction is parameterized by the hyperfine $\mathbf{A}$ tensor, and therefore, an additional term is required in the effective-spin Hamiltonian:

$$H_{\text{Er-167}} = \mu_B \mathbf{S} \cdot \mathbf{g} \cdot \mathbf{B_0} + \mathbf{S} \cdot \mathbf{A} \cdot \mathbf{I}.$$

Note that we have neglected the weak magnetic-nuclear and nuclear-quadrupole interactions in the ^{167}Er spin Hamiltonian [28] because the additional precision awarded by these terms is not required to describe the processes studied here. Meanwhile, the $\mathbf{A}$ tensor once again reflects the symmetry of the $CaWO_4$ matrix with $A_{aa} = A_{bb} = -873$ MHz and $A_{cc} = -130$ MHz, and the Hamiltonian $H_{\text{Er-167}}$ yields a total of 16 energy levels. The energy level diagrams for both H_Z and $H_{\text{Er-167}}$ are presented in the bottom panel of Fig. 2 for small magnetic fields applied perpendicular to the crystal c axis.

III. EXPERIMENTAL SETUP

For these measurements we use an ESR spectrometer comprising a thin-film superconducting resonator and a Josephson traveling wave parametric amplifier (JTWPA) [29]. Such spectrometers were described in detail in Refs. [30,31] and achieve sensitivities as high as 12 spins/$\sqrt{\text{Hz}}$ for detecting two-pulse (Hahn) echoes originating from donors in silicon at millikelvin temperatures [13]. This high sensitivity is due to the very low output noise, which is dominated by quantum fluctuations of the microwave field with little contribution from thermal photons at millikelvin temperatures. A three-dimensional perspective representation of the sample studied here is shown in Fig. 1(b). The circuit is etched into a 100 nm Nb layer sputtered directly on the surface of the $CaWO_4$ crystal, which was grown by Scientific Materials Corp. and has dimensions $0.4 \times 3 \times 6$ mm^3 parallel to the $a \times b \times c$ axes of the crystal. The superconducting LC resonator comprises 15 interdigitated fingers (the capacitor) on either side of the $725 \times 5\,\mu m^2$ wire (the inductor).

The frequency of the fundamental resonator mode is $\omega_r/2\pi = 4.37$ GHz in the absence of a magnetic field, with a quality factor $Q = 8 \times 10^3$. The resonator Q is determined by the coupling rate to the measurement line $\kappa_C = 3 \times 10^6\ s^{-1}$ and the internal energy loss rate $\kappa_i = 5 \times 10^5\ s^{-1}$. For these experiments a DC magnetic field B_0 is applied parallel to the sample surface in the direction of the inductance wire (the crystal b axis). Precision alignment of the magnetic field with respect to the crystal surface is important for minimizing the internal loss rate κ_i because field penetration into the superconducting thin film generates magnetic vortices, a well-known microwave loss channel [32].

To achieve this precision alignment, the sample is enclosed within a small copper box and mounted onto two copper-beryllium actuators from Attocube, comprising a goniometer and rotator. These are inserted into a set of two Helmholtz coils and thermally anchored to the mixing chamber (MXC) of a dilution refrigerator. While the actuators precisely orient the sample with respect to the applied magnetic field, they also create a weak thermal bridge due to the separation of metallic components by their piezoelectric elements, and therefore,

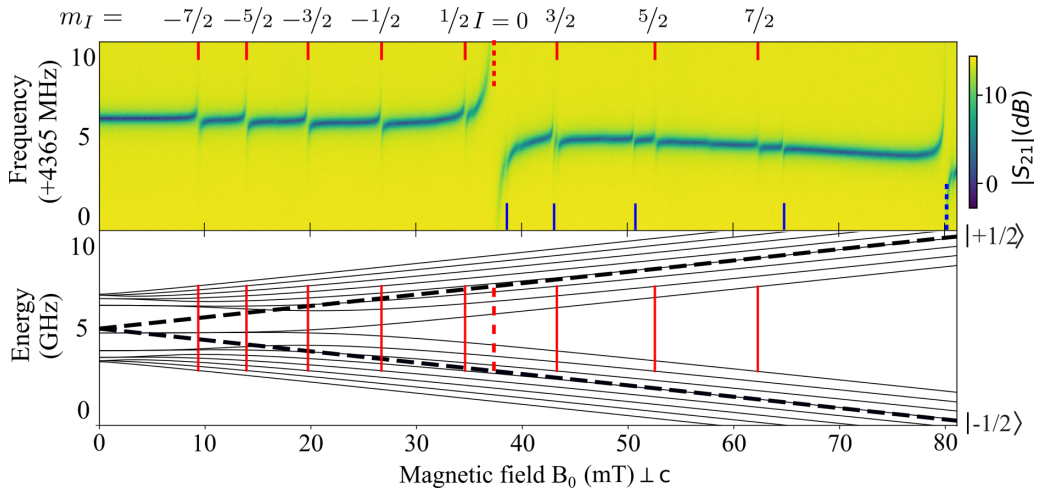

FIG. 2. Top: ESR spectrum measured at 100 mK. At this temperature all eight ESR transitions of ^{167}Er are populated, and they are labeled and indicated by vertical red lines at the top of the spectrum. The $m_I = +3/2$ transition studied here is just right of the large Er $I = 0$ transition, marked by the vertical red dashed line. Five additional ESR transitions of Yb are indicated by vertical blue lines at the bottom of the spectrum. The Yb $I = 0$ transition at 80 mT (blue dashed line) is particularly important due to its SD contribution at low temperatures. The four weaker Yb lines at lower field are attributed to the isotopes ^{171}Yb and ^{173}Yb with nuclear spins $I = 1/2$ and $I = 5/2$, respectively. Meanwhile, two additional high-field Yb lines (not shown here) are visible in the magnetic rotation spectrum presented in the Supplemental Material [33]. Bottom: Energy level diagram of ^{167}Er (solid black lines) and of Er $I = 0$ (black dashed lines). The energy levels of ^{167}Er are designated by spin-state projections $|m_S, m_I\rangle$ with the two m_S multiplets labeled on the right. The ESR transitions of Er identified in the spectrum above are marked correspondingly in red.

additional copper braiding is used between the sample box and MXC assembly to maintain good thermal conductivity.

Erbium electron-spin transitions are excited with microwave signals sent from a heavily attenuated (50 dB) input line. The transmitted microwave signal, together with the signal emitted by the spin ensemble, is then amplified by the JTWPA [see Fig. 1(b)]. Further microwave amplification takes place at 4 K using a high electron mobility transistor and at room temperature using low-noise semiconductor amplifiers.

IV. ESR SPECTROSCOPY

This crystal demonstrates a rich ESR spectrum due to the existence of several Er isotopes in natural abundance. Shown in Fig. 2, the microwave transmission spectrum is measured as a function of magnetic field applied along the crystal b axis. Note that this spectrum was recorded at an elevated temperature of 100 mK in order to populate all the hyperfine levels of ^{167}Er.

As stated previously, however, most isotopes of Er have no nuclear spin, and the largest anticrossing at 37 mT is associated with the high concentration of $I = 0$ erbium isotopes, predominantly ^{166}Er, ^{168}Er, and ^{170}Er. Here the cooperativity C between the resonator and the spin ensemble is large ($C \approx 50$) due to the high spin density. This is considerably greater than the cooperativities achieved in previous high-efficiency microwave storage demonstrations, which ranged from 0.03 [13] to 5 [14]. As mentioned in the Introduction, transitions with high absorption (and thus large cooperativities) are desirable for efficient microwave storage and microwave-to-optical transduction. Unfortunately, the high density of spins also gives rise to large instantaneous diffusion (ID), making it difficult to measure SD using the $I = 0$ transition [33]. To avoid this technical limitation, we instead focus on the low-density ^{167}Er isotope, which exhibits 16 hyperfine levels. The ESR-allowed $\Delta m_I = 0$ transitions between these levels are labeled in Fig. 2 according to their nuclear-spin projection $|m_I\rangle$. The eight corresponding solid red lines indicate the values of B_0 for which the ESR frequencies of ^{167}Er are equal to ω_r, both experimentally (Fig. 2, top) and theoretically (Fig. 2, bottom). Avoided level crossings are observed in the spectrum at these field values, which is consistent with high cooperativity between the resonator and each transition [34,35]. Additionally, the five avoided level crossings observed in the spectrum above 38 mT are attributed to Yb impurities. The large anticrossing at 80 mT is attributed to the $I = 0$ Yb isotopes, comprising all the even-numbered isotopes between ^{168}Yb and ^{176}Yb.

V. SPECTRAL DIFFUSION MODEL

We use both two-pulse echoes (2PEs) and three-pulse echoes (3PEs) to elucidate the dynamic interactions which cause SD within the $m_I = |+3/2\rangle$ spin ensemble of the ^{167}Er isotope. Here the 2PE consists of a $\pi/2$ pulse followed by a π pulse at time delay τ, while the 3PE consists of three $\pi/2$ pulses with separations τ and T_W between pulses 1 and 2 and 2 and 3, respectively. The 2PE and 3PE data yield complementary information and were first used in the 1960s by Mims, Nasau, and McGee to study SD of paramagnetic rare-earth ion impurities [36].

Since then, the theory of spectral diffusion has evolved considerably, and here we fit the 2PE and 3PE data using the uncorrelated-sudden-jump model first described by Hu and Hartmann in 1974 [37]. This model is known to yield

accurate fits of optical 2PE and 3PE data in rare-earth ion doped materials [38] and relies on four key assumptions:

(1) The subsets of the $m_I = |+3/2\rangle$ transition under investigation (the excited spins) are sufficiently isolated from each other such that they do not contribute to SD.

(2) SD is instead caused exclusively by the magnetic dipole interaction with other denser baths of perturbing spins.

(3) These perturbing spins are randomly located within the crystal matrix and exhibit only two energy configurations, i.e., a spin-1/2 system.

(4) Spin flips within the baths of perturbing spins are uncorrelated, so each flip is treated independently. To describe explicitly this model of SD we utilize the formalism first introduced by Bai and Fayer [39] and later summarized by Böttger et al. in a single equation suitable for both 2P and 3P echoes [38]. From this model, we derive a similar echo amplitude decay A_E as a function of the interpulse delays, extended to account for several species S of perturbing spins:

$$A_E = V_{\mathrm{ESEEM}} A_0 \exp\left(-2\pi\Gamma_{\mathrm{eff}}\tau\right)\exp\left(\frac{-T_W}{T_1}\right), \tag{1}$$

$$\Gamma_{\mathrm{eff}} = \Gamma_0 + \sum_S \frac{\Gamma^S_{\mathrm{SD}}}{2}\{R^S\tau + 1 - \exp(-R^S T_W)\}. \tag{2}$$

Here A_0 represents the limiting echo amplitude at zero delay, and $V_{\mathrm{ESEEM}}(\tau, T_W)$ corresponds to the electron spin echo envelope modulation (ESEEM) caused by the magnetic dipole-dipole interaction of the Er electron spins and the proximal ^{183}W nuclear spins. This is a well-defined temporal modulation that depends only on the orientation and magnitude of the applied magnetic field and has already been determined experimentally for the $m_I = |+3/2\rangle$ electron-spin transition studied here [40].

Meanwhile, the decaying component of the echo signal contains the coefficients Γ_0, Γ^S_{SD}, R^S, and T_1. The coefficient Γ_0 represents decoherence processes which occur on faster timescales than the measurement and ID caused by the microwave excitation pulses. This is equivalent to the homogeneous linewidth of a single spin transition in the absence of spectral diffusion. Conversely, Γ^S_{SD} and R^S describe the spectral diffusion which occurs due to spin species S during the delays τ and T_W (note that $T_W = 0$ in the case of 2PEs). More specifically, R^S represents the average spin-flip rate, and Γ^S_{SD} is the FWHM contribution to the dynamic distribution of transition frequencies within the $m_I = |+3/2\rangle$ subensemble.

Indeed, any paramagnetic species or ESR transition that exhibits parts per million or higher concentration can contribute significant amounts of spectral diffusion, and therefore, it is important to identify all paramagnetic impurities in the material and determine their concentration. Initially, this was attempted via magnetic rotation spectroscopy combined with numerical spin-resonator coupling estimates [33] which identified both Yb^{3+} and Mn^{2+} impurities.

However, our quantum-limited spectrometer was not able to detect paramagnetic impurities with small g factors or long spin-lattice relaxation rates due to the limited magnetic field (400 mT) and temperature (600 mK). Thus, a piece of the $CaWO_4$ boule was submitted for inductively coupled plasma–mass spectrometry analysis, and the results are presented in Table I.

Mass spectrometry allowed for the concentration of the previously identified Er, Yb, and Mn impurities to be determined with high precision, and three additional rare-earth ion impurities were also identified in the crystal at lower concentrations.

The two ESR transitions with the greatest absorption, the $I = 0$ Er and Yb transitions, were therefore included in the SD analysis. For each transition (i.e., species) S, the linewidth Γ^S_{SD} is proportional to the number of spins which can undergo spin flip, and the expected temperature dependence is described by Boltzmann statistics [38]:

$$\Gamma^S_{\mathrm{SD}}(T) = \Gamma^S_{\mathrm{max}}\,\mathrm{sech}^2\left(\frac{g_S\mu_B B_0}{2kT_B}\right), \tag{3}$$

where k is the Boltzmann constant, T_B is the electron-spin bath temperature, and g_S is the g factor of the electron-spin transition in the direction of the applied field B_0. The constant Γ^S_{max} is the maximum dynamic linewidth contribution from species S. In the high-temperature limit Γ^S_{SD} approaches Γ^S_{max} asymptotically, as the spin-down and spin-up populations of species S equalize and the magnetic-dipole interaction with the $m_I = |+3/2\rangle$ subensemble is maximized. Meanwhile, R^S is the associated rate of spin flips (the sum of upward and and downward spin flips), which is also temperature dependent and has two contributions for the studied temperature range. The first is due to the spin flip-flops, which follow the same temperature dependence as in Eq. (3). The second is the spin-lattice (phonon) interaction resonant with the spin-transition frequency $\omega_S = \mu_B g_S B_0/\hbar$, yielding the following equation [38,41]:

$$R^S(T) = \alpha_{\mathrm{ff}}\frac{g_{S\perp}{}^4 n_S^2}{\Gamma_S}\mathrm{sech}^2\left(\frac{g_S\mu_B B_0}{2kT_B}\right) + \alpha_{\mathrm{ph}} g_S^3 B_0^5 \coth\left(\frac{g_S\mu_B B_0}{2kT_B}\right). \tag{4}$$

Here α_{ff} and α_{ph} represent scaling constants of the flip-flop and spin-lattice interactions, respectively, and it is assumed they do not vary between different paramagnetic species in the crystal. Meanwhile, n_S represents the density of species S, and Γ_S is the FWHM of the inhomogeneously broadened ESR absorption line, which can depend on both the magnitude and direction of the applied magnetic field. Additionally, g_S represents the g factor in the direction of the applied field, while $g_{S\perp}$ is the g factor in the direction orthogonal to the c axis of the crystal. Note that the flip-flop rate is sensitive to only the components of the g tensor perpendicular to the direction of the applied field [42]. Here the magnetic field is applied along the b axis of the crystal, so this coupling depends on the spectroscopic splitting factors in the directions of both the a and c axes, namely, $g_\perp$ and $g_\parallel$. As $g_\parallel \ll g_\perp$ for both erbium and ytterbium, we approximate this angular dependence using only $g_\perp$ in the expression for the flip-flop rate.

In the limit $T_W = 0$, the effective linewidth presented in Eq (2) simplifies to $\Gamma_0 + \tau/2\sum\Gamma^S_{\mathrm{SD}}R^S$. Thus, it is impossible to obtain independent values for Γ_{SD} and R with only 2PE measurements due to the multiplicative relationship between

TABLE I. Calcium-relative impurity concentrations detected in a dissolved (aqueous) sample of the $CaWO_4$ boule, represented by relative mass concentration (first row) and the equivalent relative doping concentration (second row). This measurement was performed at the European Centre for Environmental Geoscience Research and Teaching using a Perkin Elmer NexION 300X mass spectrometer.

	Element					
	Mn	Ce	Nd	Gd	Er	Yb
Concentration (μg/g)	0.542	0.424	0.211	0.066	13.292	8.516
Concentration (ppm)	2.840	0.871	0.421	0.120	22.88	14.17

these two parameters. For this reason 3PE measurements are necessary to obtain an independent fit of Γ_{SD} and R.

VI. ENSEMBLE COUPLING MEASUREMENTS

To accurately fit the temperature dependence of Γ_{SD} and R it is also important to know the temperature T_B of the electron-spin bath, as this can be higher than the temperature of the mixing chamber T_{MXC} due to limited thermal conduction. Here we independently determine T_B as a function of T_{MXC} by evaluating the coupling of the $m_I = |+3/2\rangle$ subensemble to the resonator at each measured temperature, using a well-established complex transmission formula [45]:

$$S_{21}(\omega) = 1 - \frac{\kappa_C}{2i(\omega - \omega_r) + \kappa_T + \sum_S \frac{2(2\pi g_{ens}^S)^2}{i(\omega-\omega_S)+\pi\Gamma_S}}, \quad (5)$$

where g_{ens}^S is the temperature-dependent ensemble coupling between the electron-spin species S and the resonator and the other variables are as previously defined. Example fits of g_{ens}^S and Γ_S are presented in the Supplemental Material for several Er and Yb transitions [33]. Figure 3 presents the results of this fitting as a function of T_{MXC} for three of the electron-spin transitions presented in Fig. 2, the $|+1/2\rangle$, $I = 0$, and $|+3/2\rangle$ transitions.

Noting that g_{ens}^S is proportional to the square root of the electron-spin polarization of species S [45], we can directly compare the fitted ensemble coupling at each measured temperature with the expected temperature dependence, assuming the Er electron- and nuclear-spin populations thermalize to T_{MXC} according to Boltzmann statistics [33].

Indeed, the solid black lines in Fig. 3(a) represent a simultaneous fit to g_{ens}^S for all three transitions. The only free parameter in this fit is the paramagnetic Er^{3+} concentration, which yields 2×10^{17} spins/cm^3, equivalent to 18 ppm substitutional doping. This is consistent with the total Er concentration determined by mass spectrometry (Table I) which was used for the analysis of the 3PE measurements [33]. This analysis further indicates that most erbium and ytterbium ions must exist in the paramagnetic 3+ oxide state (as opposed to the 2+ and 4+ states), and the high degree of chemical similarity between the rare-earth ions would further imply that the total concentrations presented in Table I also yield the total paramagnetic ion concentration in the crystal, with the exception of [Mn^{2+}].

Figure 3(b) presents an enlarged view of the ensemble-coupling data and a fit for the $m_I = |+3/2\rangle$ transition. This transition was chosen to probe the spin temperature below 100 mK because the nuclear-spin distribution of ^{167}Er is considerably more sensitive to heating in this temperature region than the electron-spin distribution of the $I = 0$ Er isotopes, shown by the green curve in Fig. 3(a). Moreover, we assume that this measurement of the hyperfine level temperature of ^{167}Er accurately determines the electron-spin bath temperature T_B of all paramagnetic impurities in the sample because of the strong hyperfine coupling between the electronic and nuclear spins of ^{167}Er, which keeps both spin baths isothermal. In particular, the fit to the data in Fig. 3(b) suggests that T_B is well approximated by T_{MXC} above 30 mK. Below this MXC temperature, however, we infer that poor thermal conduction combined with some heating at or near the location of the sample leads to an elevated bath temperature

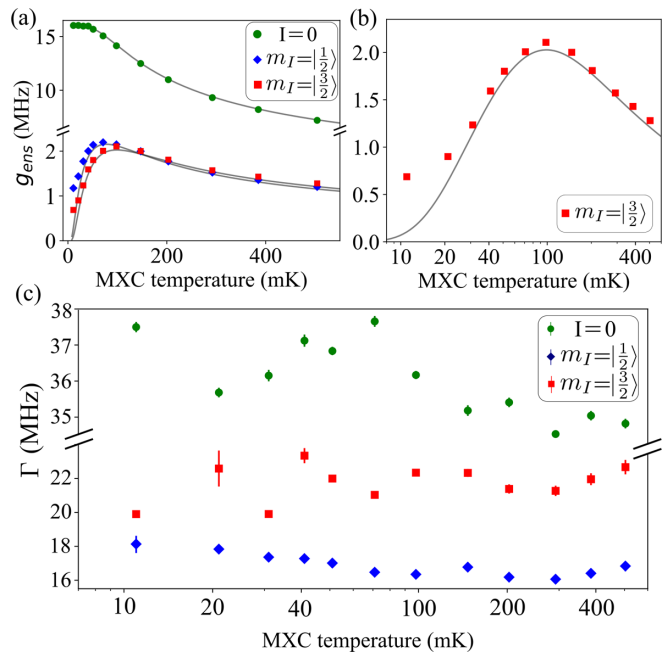

FIG. 3. Ensemble coupling and inhomogeneous linewidths as a function of MXC temperature, determined using a fit to Eq. (5) for three electron-spin transitions of Er: the $I = 0$ transition (green) and the $m_I = |\frac{1}{2}\rangle$ (blue) and $m_I = |\frac{3}{2}\rangle$ (red) transitions of ^{167}Er. (a) g_{ens} values extracted from the fit (colored dots). The solid black lines show a simultaneous fit to all three g_{ens} data sets assuming a thermal Boltzmann distribution of spin levels. (b) Same data as in (a) for the $m_I = |\frac{3}{2}\rangle$ transition, presented with a logarithmic temperature scale. (c) Inhomogeneous linewidths Γ extracted from the same fitting as in (a) presented with a logarithmic temperature scale. Here a negligible temperature dependence is observed for all three transitions, consistent with the observation that inhomogeneous broadening of paramagnetic impurities is dominated by electrostatic perturbations in $CaWO_4$ [43,44].

with $T_B = 23 \pm 2$ mK at $T_{\mathrm{MXC}} = 11$ mK and $T_B = 27 \pm 2$ mK when $T_{\mathrm{MXC}} = 21$ mK.

Both the excess heating and poor conductivity are likely caused by the piezoelectric actuators that precisely align the sample in the applied magnetic field. The issue of poor thermal conductivity was mentioned in Sec. II, and the frictional "stick-slip" mechanism which moves the actuators could potentially be a heat source even during static (nonmoving) operation [46]. This is possible if vibrations from the pulse-tube cooler couple to the loose frictional surfaces within the actuators, which are required for precise displacement. Indeed, thermal excursions up to 100 mK were observed when the actuators were actively displaced using a voltage signal, and this temperature rise is attributed to frictional heating.

VII. ECHO MEASUREMENTS

As mentioned at the beginning of Sec. V, 2PE and 3PE measurements were recorded at various spin-bath temperatures T_B to determine the SD parameters Γ^S_{SD} and R^S. A selection of these measurements is presented in Fig. 4. To accurately determine the echo decay rates, it was necessary to fit the large ESEEM modulation depths observed in Figs. 4(a) and 4(b). Fortunately, the ESEEM parameters have already been measured and published for the sample and experimental configuration used here [40].

For the 3PE measurements, up to 10 decay curves were taken at five different temperatures as a function of T_W, with fixed τ ranging from 6 to 96 μs. These small values of τ were chosen for the 3PE measurements because they allow for accurate estimates of the rapid SD at higher temperatures. An example set of 3PE curves recorded at 530 and 27 mK is presented in Figs. 4(c) and 4(d), respectively. ESEEM is also present and simulated for the 3PE decay curves; however, the data were recorded with large T_W spacings, so the fitted curves in gray show an undersampling of the modulation. As mentioned previously, we rely on 3PE data to determine R and Γ_{SD} at each measured temperature because 2PE measurements cannot be used to fit these two parameters independently. For this fitting we also consider only the flip-flop contribution of $R^S(T)$ and the relative concentrations of Er and Yb impurities. The result of this fitting is presented in Figs. 5(a) and 5(b), and the details of the fitting process are presented in the Supplemental Material [33]. For both the 2PE and 3PE measurements it is then possible to define a coherence time,

$$T_2 = \frac{-a + \sqrt{a^2 + 2b/\pi}}{b}. \tag{6}$$

Here $a = \Gamma_0$, and $b = \frac{1}{2}\sum_S \Gamma^S_{\mathrm{SD}} R^S$. These two parameters arise from the quadratic exponent $\Gamma_{\mathrm{eff}}\tau = a\tau + b\tau^2$ presented in Eq. (2) when $T_W = 0$. For both the 2PE and 3PE measurements, this value of T_2 represents the time 2τ when the echo has decayed to e^{-1} of its initial amplitude (in the limit $T_W = 0$ for 3PE measurements) and is presented in Fig. 5(c).

Above 100 mK the values of T_2 inferred from 2PE and 3PE measurements agree within error. However, they diverge below this temperature due to the difficulty in determining T_2 accurately using 3PE measurements when $T_2 \gg \tau$. Instead, the long tail of the T_W-dependent decay visible in Figs. 4(c) and 4(d) is sensitive to spectral-diffusion processes that occur on timescales much longer than T_2. For this reason we rely solely on the 2PE fit to determine T_2 at the lowest spin-bath temperatures, and we observe a maximum value of $T_2 = 1.3 \pm 0.1$ ms at $T_B = 23$ mK.

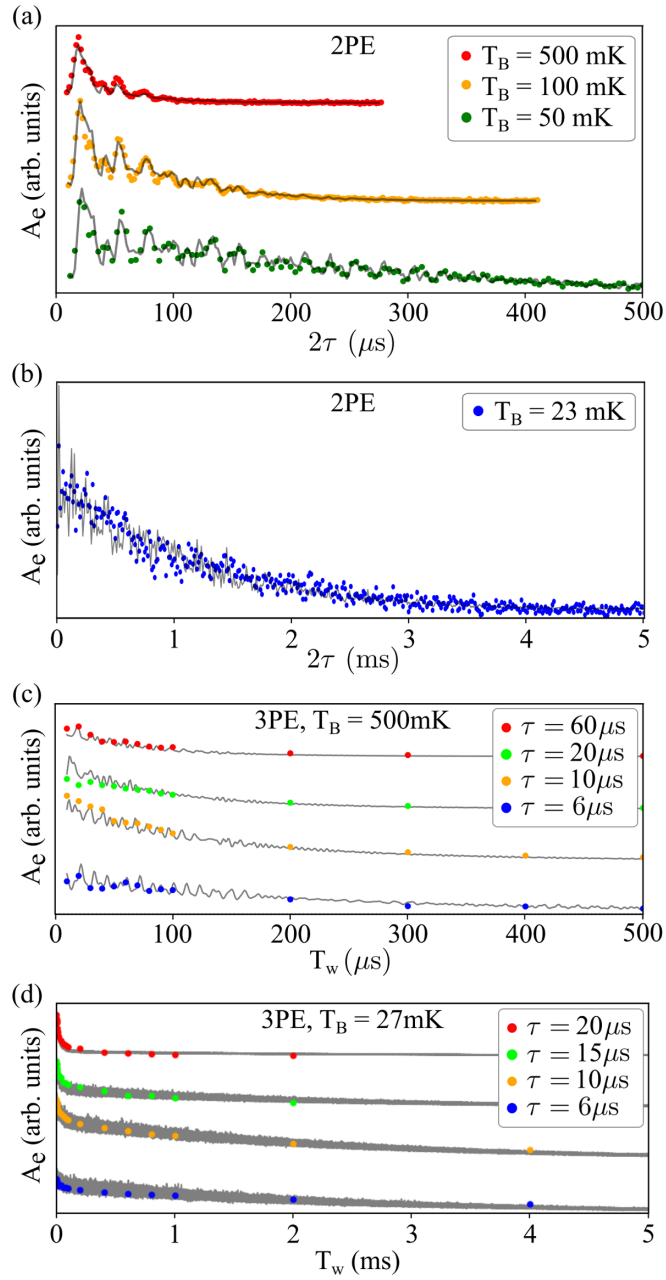

FIG. 4. Two- and three-pulse echo decay curves (colored dots) measured as a function of delay times τ or T_W and their respective fits (gray solid curves). (a) Waterfall plot of two-pulse echo decay curves measured in the temperature range of 50–500 mK. (b) Two-pulse echo measurement recorded at $T_B = 23$ mK, the lowest achievable spin-bath temperature for the experiments performed here. (c) Waterfall plot of three-pulse echo decay curves measured at $T_B = 530$ mK as a function of both τ and T_W time delays. (d) Waterfall plot of three-pulse echo decay curves measured at $T_B = 27$ mK.

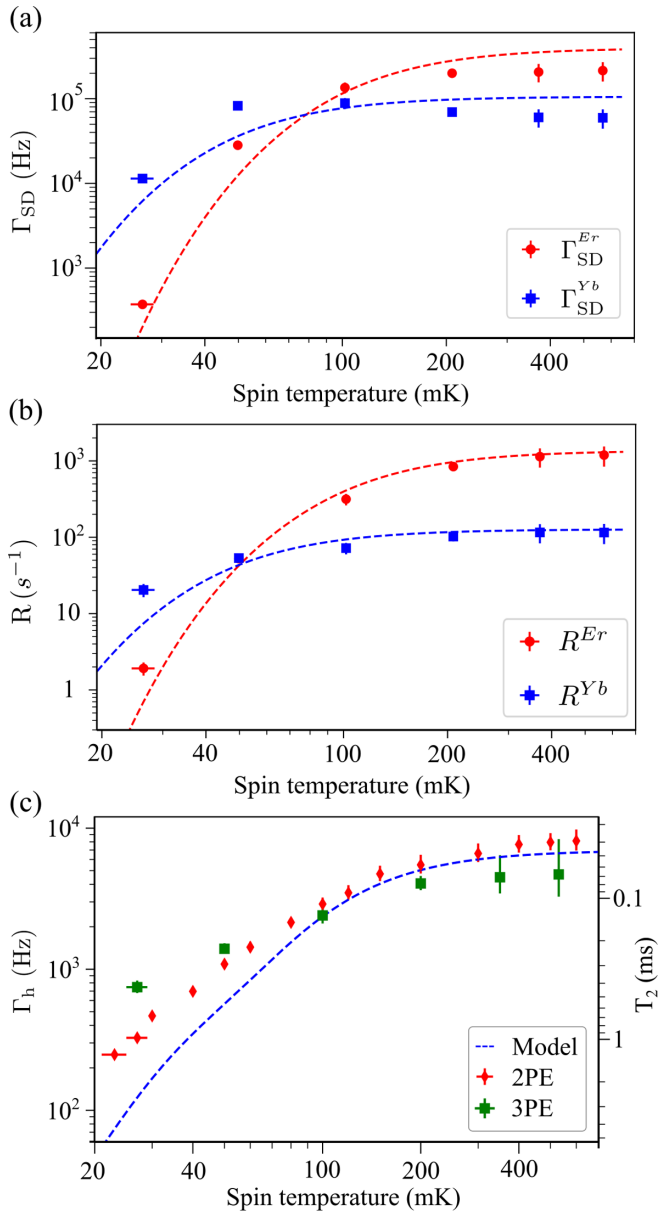

FIG. 5. Spectral diffusion and decoherence rates. (a) Linewidth Γ_{SD} and (b) spin-flip rates R^S extracted from 3PE fits to Eq. (1) for six temperatures and two spin species. X (Y) error bars show standard error in the fit to the spin-bath temperature (spin-flip rate and linewidth). Red (blue) dashed lines in (a) and (b) represent fits to Eqs. (3) and (4) for Er (Yb), respectively. (c) Extracted coherence time T_2 (right-hand side) and equivalent effective decoherence rate $\Gamma_h = 1/\pi T_2$ (left-hand side) from the 2PE data (red) and the 3PE data (green). The decoherence model (blue dashed line) takes into account the SD parameters extracted from the 3PE measurements, the ID of the $m_I = |+3/2\rangle$ transition, and the dephasing caused by the unpolarized ^{183}W nuclear-spin bath.

VIII. ANALYSIS

Figures 5(a) and 5(b) illustrate the large decrease in Γ_{SD} and R with decreasing temperature for both the Er and Yb spins. We attribute this to a reduction in the electron-spin flip-flop rate as a consequence of thermal polarization of the spin populations. Indeed, our *a priori* neglect of the spin-lattice contribution in our SD analysis (see the Supplemental Material [33]) is justified by the rapid spin-flip rates observed across the studied temperature range. For instance, R^{Er} is orders of magnitude greater than the spin-lattice relaxation rate $T_1^{-1} = 0.01\ s^{-1}$ estimated from previous measurements of spin-lattice relaxation in Er:$CaWO_4$ at 7.88 GHz and 500 mK [21], given the $g_S^3 B_0^5$ scaling presented in Eq. (4).

While flip-flops within the Er electronic-spin bath are clearly the dominant source of SD at high temperature, the Yb electron spins contribute most to SD at $T_B = 23$ mK. This occurs because the Yb spins are less thermally polarized as a consequence of their smaller g factor, even though the Yb spin bath is less dense than the Er bath. Moreover, the total experimental contribution to SD from both the Er and Yb spins at the lowest temperature is significantly greater than the expected contribution shown by the dashed-line fits in Figs. 5(a) and 5(b).

This discrepancy is also present in the decoherence-rate model presented in Fig. 5(c). This model is detailed in the Supplemental Material [33] and takes into account the expected contribution of the temperature-dependent instantaneous diffusion due to pulse excitation in addition to the dephasing caused by the ^{183}W nuclear-spin bath. Here the instantaneous diffusion contribution is temperature dependent due to the thermal population density of the $m_I = |+3/2\rangle$ hyperfine state. Using the method described in Refs. [47,48], we estimate minimum and maximum contributions of 51 Hz at 23 mK and 630 Hz at 530 mK, respectively. The temperature-independent dephasing caused by the unpolarized ^{183}W nuclear-spin bath contributes only 12 Hz, a value derived from the cluster-correlation expansion estimate of T_2 determined by Le Dantec *et al.* [21] for the Er electron-spin transition in $CaWO_4$.

The remaining discrepancy can have two possible origins. The first is the fact that the uncorrelated-sudden-jump model presented in Sec. V makes the incorrect assumption that all spin flips are uncorrelated in this system. Although this is valid for spin flips driven predominantly by spin-lattice relaxation, as has been the case in previous applications of this model [38], there is an inherent correlation between spins flips when they are driven by flip-flops. While the derivation of a "correlated-sudden-jump" model which accounts for this discrepancy is beyond the scope of this work, it would be possible to investigate this issue further by simulating flip-flops of the paramagnetic spin baths using the cluster-correlation expansion approach [49,50].

The second possibility is that one or more additional electron-spin species are contributing significantly to SD at low temperatures, consistent with the observation of additional impurities in the mass spectrum (Table I). One likely candidate species is Mn^{2+}, the third most abundant impurity in the crystal at a relative concentration of 2.8 ppm. With a g factor of 2, manganese is weakly polarized at 23 mK and has a complex electronic level structure with $S = 5/2$ and $I = 3/2$ [51]. Unfortunately, as there is no analytic expression for SD processes in an electron-spin system with $S > 1/2$, it was deemed beyond the scope of this work to derive and test one here due to the relatively low concentration of manganese. Therefore, estimates of the SD contribution of Mn^{2+} were not undertaken.

IX. CONCLUSION

Here we demonstrated an electron-spin coherence time exceeding 1 ms in 20 ppm doped Er^{3+}:$CaWO_4$, achieved by cooling the electronic spin bath to 23 mK and thereby significantly reducing the electron-spin flip-flop rate of both the Er and Yb impurities.

Further enhancements in spin coherence could be achieved by chemically and isotopically purifying the host matrix or improving the thermal spin polarization. For instance, increasing the resonator frequency from 4.4 to 8 GHz would significantly improve thermal polarization while maintaining compatibility with superconducting microwave circuits that typically operate in the 4–8 GHz band. In this situation one would expect the SD contribution of the Er and Yb spins to be reduced by factors of approximately 10^3 and 10^2, respectively, at a spin-bath temperature of 23 mK.

Chemical purification is also an important avenue to pursue because the smaller g factors of nonerbium impurities will generally lead to significant SD contributions at low temperatures. Indeed, ytterbium alone presents an SD contribution 320 times greater than erbium at 4.4 GHz and 23 mK. Reducing the Yb concentration to the parts per billion level observed in chemically purified $CaWO_4$ would reduce this contribution by seven orders of magnitude, assuming the inhomogeneous spin-transition linewidth remains largely unchanged.

While such improvements could result in coherence times approaching the ^{183}W nuclear-spin-limited T_2 of 27 ms [21] at parts per million Er concentrations, further enhancements of spin-coherence times would require isotopic enrichment. Indeed, epitaxially grown rare-earth doped thin films have already been considered for this purpose [52], partly because the cost of isotopically enriched oxide required for macroscopic crystal boules is prohibitive. Although simulations of spin coherence in a ^{183}W-free Scheelite crystal have not yet been undertaken, cluster-correlated-expansion estimates of spin coherence in natural materials devoid of tungsten (such as CaO) suggest that significant enhancements in spin coherence times might be achieved once the dense ^{183}W nuclear-spin bath is eliminated [22].

ACKNOWLEDGMENTS

We acknowledge technical support from P. Sénat, D. Duet, P.-F. Orfila, and S. Delprat, and we are grateful for fruitful discussions within the Quantronics group. We acknowledge IARPA and Lincoln Labs for providing the Josephson traveling-wave parametric amplifier. This project has received funding from the European Union's Horizon 2020 research and innovation program under Marie Sklodowska-Curie Grants Agreement No. 765267 (QuSCO) and No. 792727 (SMERC). E.F. acknowledges support from Agence Nationale de la Recherche (ANR) Grant No. DARKWADOR:ANR-19-CE47-0004. We acknowledge support from the ANR through the Chaire Industrielle NASNIQ under Contract No. ANR-17-CHIN-0001 cofunded by Atos and through the project MIRESPIN under Contract No. ANR-19-CE47-0011 and of the Region Ile-de-France through the DIM SIRTEQ (REIMIC project). We acknowledge support of the AIDAS virtual joint laboratory. R.B.L. was supported by the Hong Kong Research Grants Council - General Research Fund (Project No. 14302121). S.L. was supported by the Impact Postdoctoral Fellowship of CUHK. S.B. acknowledges the support of the CNRS research infrastructure INFRANALYTICS (FR2054).

[1] M. Zhong, M. P. Hedges, R. L. Ahlefeldt, J. G. Bartholomew, S. E. Beavan, S. M. Wittig, J. J. Longdell, and M. J. Sellars, Optically addressable nuclear spins in a solid with a six-hour coherence time, Nature (London) **517**, 177 (2015).

[2] A. Holzäpfel, J. Etesse, K. T. Kaczmarek, A. Tiranov, N. Gisin, and M. Afzelius, Optical storage for 0.53 s in a solid-state atomic frequency comb memory using dynamical decoupling, New J. Phys. **22**, 063009 (2020).

[3] J. J. Longdell, E. Fraval, M. J. Sellars, and N. B. Manson, Stopped Light with Storage Times Greater than One Second Using Electromagnetically Induced Transparency in a Solid, Phys. Rev. Lett. **95**, 063601 (2005).

[4] M. Rančić, M. P. Hedges, R. L. Ahlefeldt, and M. J. Sellars, Coherence time of over a second in a telecom-compatible quantum memory storage material, Nat. Phys. **14**, 50 (2018).

[5] M. P. Hedges, J. J. Longdell, Y. Li, and M. J. Sellars, Efficient quantum memory for light, Nature (London) **465**, 1052 (2010).

[6] J. Dajczgewand, J.-L. Le Gouët, A. Louchet-Chauvet, and T. Chanelière, Large efficiency at telecom wavelength for optical quantum memories, Opt. Lett. **39**, 2711 (2014).

[7] M. Sabooni, Q. Li, S. Kröll, and L. Rippe, Efficient Quantum Memory Using a Weakly Absorbing Sample, Phys. Rev. Lett. **110**, 133604 (2013).

[8] J. G. Bartholomew, J. Rochman, T. Xie, J. M. Kindem, A. Ruskuc, I. Craiciu, M. Lei, and A. Faraon, On-chip coherent microwave-to-optical transduction mediated by ytterbium in YVO4, Nat. Commun. **11**, 3266 (2020).

[9] X. Fernandez-Gonzalvo, S. P. Horvath, Y. H. Chen, and J. J. Longdell, Cavity-enhanced Raman heterodyne spectroscopy in Er^{3+}:Y_2SiO_5 for microwave to optical signal conversion, Phys. Rev. A **100**, 033807 (2019).

[10] C. Grezes, Y. Kubo, B. Julsgaard, T. Umeda, J. Isoya, H. Sumiya, H. Abe, S. Onoda, T. Ohshima, K. Nakamura, I. Diniz, A. Auffeves, V. Jacques, J. F. Roch, D. Vion, D. Esteve, K. Moelmer, and P. Bertet, Towards a spin-ensemble quantum memory for superconducting qubits, C. R. Phys. **17**, 693 (2016).

[11] A. J. Sigillito, H. Malissa, A. M. Tyryshkin, H. Riemann, N. V. Abrosimov, P. Becker, H. J. Pohl, M. L. Thewalt, K. M. Itoh, J. J. Morton, A. A. Houck, D. I. Schuster, and S. A. Lyon, Fast, low-power manipulation of spin ensembles in superconducting microresonators, Appl. Phys. Lett. **104**, 222407 (2014).

[12] C. Grèzes, Towards a spin ensemble quantum memory for superconducting qubits, Ph.D. thesis, Université Paris-Saclay, 2015.

[13] V. Ranjan, S. Probst, B. Albanese, T. Schenkel, D. Vion, D. Esteve, J. J. L. Morton, and P. Bertet, Electron spin resonance

spectroscopy with femtoliter detection volume, Appl. Phys. Lett. **116**, 184002 (2020).

[14] S. Probst, H. Rotzinger, A. V. Ustinov, and P. A. Bushev, Microwave multimode memory with an erbium spin ensemble, Phys. Rev. B **92**, 014421 (2015).

[15] A. G. Fowler, D. S. Wang, C. D. Hill, T. D. Ladd, R. Van Meter, and L. C. L. Hollenberg, Surface Code Quantum Communication, Phys. Rev. Lett. **104**, 180503 (2010).

[16] A. G. Fowler, M. Mariantoni, J. M. Martinis, and A. N. Cleland, Surface codes: Towards practical large-scale quantum computation, Phys. Rev. A **86**, 032324 (2012).

[17] G. Dold, Millikelvin ESR of rare-earth doped crystals using superconducting resonators, Ph.D. thesis, University College London, 2020.

[18] P. Y. Li, C. Liu, Z. Q. Zhou, X. Liu, T. Tu, T. S. Yang, Z. F. Li, Y. Ma, J. Hu, P. J. Liang, X. Li, J. Y. Huang, T. X. Zhu, C. F. Li, and G. C. Guo, Hyperfine Structure and Coherent Dynamics of Rare-Earth Spins Explored with Electron-Nuclear Double Resonance at Subkelvin Temperatures, Phys. Rev. Appl. **13**, 024080 (2020).

[19] J. V. Rakonjac, Y.-H. Chen, S. P. Horvath, and J. J. Longdell, Long spin coherence times in the ground state and in an optically excited state of $^{167}Er^{3+}:Y_2SiO_5$ at zero magnetic fields, Phys. Rev. B **101**, 184430 (2020).

[20] A. Ortu, A. Tiranov, S. Welinski, F. Fröwis, N. Gisin, A. Ferrier, P. Goldner, and M. Afzelius, Simultaneous coherence enhancement of optical and microwave transitions in solid-state electronic spins, Nat. Mater. **17**, 671 (2018).

[21] M. Le Dantec, M. Rančić, S. Lin, E. Billaud, V. Ranjan, D. Flanigan, S. Bertaina, T. Chanelière, P. Goldner, A. Erb, R. B. Liu, D. Estève, D. Vion, E. Flurin, and P. Bertet, Twenty-three millisecond electron spin coherence of erbium ions in a natural-abundance crystal, Sci. Adv. **7**, eabj9786 (2021).

[22] S. Kanai, F. J. Heremans, H. Seo, G. Wolfowicz, C. P. Anderson, S. E. Sullivan, M. Onizhuk, G. Galli, D. D. Awschalom, and H. Ohno, Generalized scaling of spin qubit coherence in over 12,000 host materials, Proc. Natl. Acad. Sci. USA **119**, e2121808119 (2022).

[23] B. Herzog and E. L. Hahn, Transient nuclear induction and double nuclear resonance in solids, Phys. Rev. **103**, 148 (1956).

[24] A. M. Ferrenti, N. P. de Leon, J. D. Thompson, and R. J. Cava, Identifying candidate hosts for quantum defects via data mining, npj Comput. Mater. **6**, 126 (2020).

[25] A. Kiel and W. B. Mims, Electric-field-induced *g* shifts for loose Yb ions in three scheelite lattices, Phys. Rev. B **1**, 2935 (1970).

[26] B. G. Enrique, Optical spectrum and magnetic properties of Er^{3+} in $CaWO_4$, J. Chem. Phys. **55**, 2538 (1971).

[27] S. Bertaina, S. Gambarelli, A. Tkachuk, I. N. Kurkin, B. Malkin, A. Stepanov, and B. Barbara, Rare-earth solid-state qubits, Nat. Nanotechnol. **2**, 39 (2007).

[28] O. Guillot-Noël, P. Goldner, Y. L. Du, E. Baldit, P. Monnier, and K. Bencheikh, Hyperfine interaction of Er^{3+} ions in $Y_2 : SiO_5$: An electron paramagnetic resonance spectroscopy study, Phys. Rev. B **74**, 214409 (2006).

[29] C. Macklin, K. O'Brien, D. Hover, M. E. Schwartz, V. Bolkhovsky, X. Zhang, W. D. Oliver, and I. Siddiqi, A near-quantum-limited Josephson traveling-wave parametric amplifier, Science **350**, 307 (2015).

[30] S. Probst, A. Bienfait, P. Campagne-Ibarcq, J. J. Pla, B. Albanese, J. F. Da Silva Barbosa, T. Schenkel, D. Vion, D. Esteve, K. Mølmer, J. J. Morton, R. Heeres, and P. Bertet, Inductive-detection electron-spin resonance spectroscopy with 65 spins/$\sqrt{\text{Hz}}$ sensitivity, Appl. Phys. Lett. **111**, 202604 (2017).

[31] A. Bienfait, J. J. Pla, Y. Kubo, M. Stern, X. Zhou, C. C. Lo, C. D. Weis, T. Schenkel, M. L. W. Thewalt, D. Vion, D. Esteve, B. Julsgaard, K. Moelmer, J. J. L. Morton, P. Bertet, K. Mølmer, J. J. L. Morton, and P. Bertet, Reaching the quantum limit of sensitivity in electron spin resonance, Nat. Nanotechnol. **11**, 253 (2016).

[32] C. Song, T. W. Heitmann, M. P. DeFeo, K. Yu, R. McDermott, M. Neeley, J. M. Martinis, and B. L. T. Plourde, Microwave response of vortices in superconducting thin films of Re and Al, Phys. Rev. B **79**, 174512 (2009).

[33] See Supplemental Material at http://link.aps.org/supplemental/10.1103/PhysRevB.106.144412 for measurements of instantaneous diffusion, a magnetic rotation spectrum, fits of transmission spectra, estimates of spin temperature, derivation of the Er^{3+} and Yb^{3+} doping concentrations, fits of the three-pulse echo data, and a decoherence-rate model.

[34] S. Probst, H. Rotzinger, S. Wünsch, P. Jung, M. Jerger, M. Siegel, A. V. Ustinov, and P. A. Bushev, Anisotropic Rare-Earth Spin Ensemble Strongly Coupled to a Superconducting Resonator, Phys. Rev. Lett. **110**, 157001 (2013).

[35] Y. Kubo, F. R. Ong, P. Bertet, D. Vion, V. Jacques, D. Zheng, A. Dréau, J.-F. Roch, A. Auffeves, F. Jelezko, J. Wrachtrup, M. F. Barthe, P. Bergonzo, and D. Esteve, Strong Coupling of a Spin Ensemble to a Superconducting Resonator, Phys. Rev. Lett. **105**, 140502 (2010).

[36] W. B. Mims, K. Nassau, and J. D. McGee, Spectral Diffusion in Electron Resonance Lines, Phys. Rev. **123**, 2059 (1961).

[37] P. Hu and S. R. Hartmann, Theory of spectral diffusion decay using an uncorrelated-sudden-jump model, Phys. Rev. B **9**, 1 (1974).

[38] T. Böttger, C. W. Thiel, Y. Sun, and R. L. Cone, Optical decoherence and spectral diffusion at 1.5 μm in $Er^{3+}:Y_2SiO_5$ versus magnetic field, temperature, and Er^{3+} concentration, Phys. Rev. B **73**, 075101 (2006).

[39] Y. S. Bai and M. D. Fayer, Time scales and optical dephasing measurements: Investigation of dynamics in complex systems, Phys. Rev. B **39**, 11066 (1989).

[40] S. Probst, G. Zhang, M. Rančić, V. Ranjan, M. Le Dantec, Z. Zhang, B. Albanese, A. Doll, R. B. Liu, J. Morton, T. Chanelière, P. Goldner, D. Vion, D. Esteve, and P. Bertet, Hyperfine spectroscopy in a quantum-limited spectrometer, Magn. Reson. **1**, 315 (2020).

[41] M. Le Dantec, Electron spin dynamics of erbium ions in scheelite crystals, probed with superconducting resonators at millikelvin temperatures, Ph.D. thesis, Université Paris-Saclay, 2022.

[42] B. Car, L. Veissier, A. Louchet-Chauvet, J. L. Le Gouët, and T. Chanelière, Optical study of the anisotropic erbium spin flip-flop dynamics, Phys. Rev. B **100**, 165107 (2019).

[43] W. B. Mims and R. Gillen, Broadening of paramagnetic-resonance lines by internal electric fields, Phys. Rev. **148**, 438 (1966).

[44] E. I. Baibekov, D. G. Zverev, I. N. Kurkin, A. A. Rodionov, B. Z. Malkin, and B. Barbara, Broadening of paramagnetic resonance lines by charged point defects in neodymium-doped scheelites, Opt. Spectrosc. **116**, 661 (2014).

[45] V. Ranjan, G. de Lange, R. Schutjens, T. Debelhoir, J. P. Groen, D. Szombati, D. J. Thoen, T. M. Klapwijk, R. Hanson, and L. DiCarlo, Probing Dynamics of an Electron-Spin Ensemble via a Superconducting Resonator, Phys. Rev. Lett. **110**, 067004 (2013).

[46] M. Zech, J. Schoebel, and T. Pickert, Stick-slip drive, especially pieze-actuated inertial drive, U.S. Patent and Trademark Office, U.S. Patent No. US 10,505,470 (2019), https://patents.google.com/patent/US10505470B2/en.

[47] V. V. Kurshev and T. Ichikawa, Effect of spin flip-flop on electron-spin-echo decay due to instantaneous diffusion, J. Magn. Reson. (1969-1992) **96**, 563 (1992).

[48] A. M. Tyryshkin, S. Tojo, J. J. Morton, H. Riemann, N. V. Abrosimov, P. Becker, H. J. Pohl, T. Schenkel, M. L. Thewalt, K. M. Itoh, and S. A. Lyon, Electron spin coherence exceeding seconds in high-purity silicon, Nat. Mater. **11**, 143 (2012).

[49] W. Yang and R. B. Liu, Quantum many-body theory of qubit decoherence in a finite-size spin bath, Phys. Rev. B **78**, 085315 (2008).

[50] W. Yang and R. B. Liu, Quantum many-body theory of qubit decoherence in a finite-size spin bath. II. Ensemble dynamics, Phys. Rev. B **79**, 115320 (2009).

[51] C. F. Hempstead and K. D. Bowers, Paramagnetic resonance of impurities in $CaWO_4$. I. Two *S*-state ions, Phys. Rev. **118**, 131 (1960).

[52] K. Shin, I. Gray, G. Marcaud, S. P. Horvath, F. J. Walker, J. D. Thompson, and C. H. Ahn, Er-doped anatase TiO_2 thin films on $LaAlO_3$ (001) for quantum interconnects (QuICs), Appl. Phys. Lett. **121**, 081902 (2022).